

Smoothed Particle Hydrodynamics coupled with Radiation Transfer

Hajime Susa

Department of Physics, Rikkyo University, Nishi-Ikebukuro, Toshimaku, Japan
susa@rikkyo.ac.jp

(Received (reception date); accepted (acceptation date))

Abstract

We have been constructed a brand-new radiation hydrodynamics solver based upon Smoothed Particle Hydrodynamics (SPH), which works on parallel computer system. The code is designed to investigate the formation and evolution of the first generation objects at $z \gtrsim 10$, where the radiative feedback from various sources play important roles. The code can compute the fraction of chemical species e, H^+ , H, H^- , H_2 , and H_2^+ by fully implicit time integration. It also can deal with multiple sources of ionizing radiation, as well as the radiation at Lyman-Werner band. We compare the results for a few test calculations with the results of one dimensional simulations, in which we find good agreements with each other. We also evaluate the speedup by parallelization, that is found to be almost ideal, as far as the number of sources is comparable to the number of processors.

Key words: *radiation transfer—hydrodynamics—galaxy formation — first stars*

1. Introduction

One of the important objectives of cosmology today is to understand the way how the first generation stars or galaxies are formed and how they affected the later structure formation, and how they reionized the surrounding media. These problems have been studied intensively in the last decade, hence we already have some knowledge on these issues. However, studies which properly address the radiation transfer effects are still at the beginning, in spite of their great importance.

In order to investigate the radiation transfer effects on such issues in realistic cosmological density field, we need the code which can deal with hydrodynamics, gravity, chemical reactions, and naturally radiation transfer in three dimension. So far, various kinds of numerical approaches have been taken by several authors at different levels. There are several codes which focusing on the fragmentation of primordial gas (Abel, Bryan, Norman 2000; Bromm, Coppi & Larson 1999; Bromm, Coppi & Larson 2002; Nakamura & Umemura 1999; Nakamura & Umemura 2001; Yoshida et al. 2003), without radiation transfer. There also are the radiation transfer codes in which hydrodynamics are not coupled (Abel, Norman & Madau 1999; Nakamoto, Umemura, & Susa 2001; Razoumov et al. 2002; Maselli, Ferrara & Ciardi 2003). Some of these codes have the merit that they can include diffuse radiation field (Nakamoto, Umemura, & Susa 2001; Razoumov et al. 2002; Maselli, Ferrara & Ciardi 2003). Utilizing this strong point, these trials can give answers to the cosmic reionization problem to some extent, however, they do not fit to investigate the problem of structure formation because of the dynamical nature of the phenomena and radiative feedback effects on star/galaxy formation. Moreover, cosmic reionization problem itself is also coupled with structure formation, since the formed stars, galaxies and black holes are the sources of reionization. Therefore we need some assumptions on the nature and number of the sources when we try to investigate the reionization of the Universe with this type of simulations.

Another approach to these issues is suggested by Gnedin & Abel (2001), in which paper they propose a new type of approximation, called as Optically Thin Variable Eddington Tensor method (OTVET). They solve the moment equations of transfer equation on the assumption that the closure relation is given by the Eddington tensor which is assessed under the optically thin approximation. The advantage of the approximation is that radiation transfer can be coupled with hydrodynamics, since this approximation reduces the computational cost dramatically. Therefore they could trace the cosmic reionization history in a self-consistent fashion.

Recently, Mellema et al. (2005) and Rijkhorst et al. (2005) have constructed fully coupled Radiation Hydrodynamics (RHD) codes applying on the cosmic reionization problem. They couple the adoptive mesh refinement hydrodynamics codes with adoptive ray-tracing codes. They successfully trace the radiation hydrodynamic expansion of HII region, as well as the formation of shadows behind dense clumps. However, their codes still do not include H_2 chemistry and transfer of Lyman-Werner band radiation, although they are crucial for the calculation of first structure formation.

Another branch of radiation hydrodynamic approach was proposed by Kessel-Deynet & Burkert (2000), in which they show a scheme of ray tracing in Smoothed Particle Hydrodynamics (SPH). SPH is often applied to the simulations

on galaxy formation and star formation, because of its Lagrange nature and simplicity. They create grid points on light rays from sources to SPH particles. The code has an advantage that the ray tracing is naturally incorporated into Lagrangian scheme, since they utilize the neighbor lists of particles to find the grid points. We have parallelized their scheme in case light rays from the source can be approximated as parallel (Susa & Umemura 2004a). However, the parallelized code cannot be applied to the problems with multiple sources, that are crucially required for the first structure formation.

In this paper, we describe the newly developed RHD code by ourselves, in which fully coupled hydrodynamics, gravity, chemical reactions with H_2 are included, as well as radiation transfer of ionizing photons and the Lyman-Werner band photons. One of the characteristic feature of this code is that we employ SPH. Radiation transfer part of the code is a natural extension of our previous code described in Susa & Umemura (2004a). Thanks to the newly developed radiation transfer and parallelization scheme, we can include multiple sources in our new code. Since it is a particle code, it also has an advantage that it has the good affinity to GRAPE system (Fukushige, Makino & Kawai 2005) which can be dedicated to the gravitational force calculations and neighbor search. We also show the outcomes of some calculations on the test problems, that are compared with the results of one dimensional simulations.

This paper is organized as follows. We describe the detail of the code in section 2. Then we show the results of test calculations in section 3, and summarize in the final section 4.

2. Code Description

In this section, we describe the basic methods of the code, dividing into several parts. First, we describe the method to evaluate gravitational force. Then, we explain how we treat hydrodynamics, radiation transfer, and thermal processes in order.

2.1. Gravity

We use a parallel version of Barnes-Hut Tree code (Barnes & Hut 1986) to assess the acceleration owing to gravitational force. The core routine of the tree code is originally provided by Jun Makino ¹, as a serial version in FORTRAN77, which is parallelized by ourselves.

The computational domain is decomposed by Orthogonal Recursive Bisection (ORB) method (Dubinski 1996). We built up the so-called local tree and locally essential tree, then walk along the tree structure to obtain the interaction list. The parallelization scheme is summarized in Figure 1. Suppose we have four processor units (PUs) whose computational domains are represented by the rectangles. Now we try to assess the acceleration on the particles in PU1. In the first step (left panel), Barnes-Hut tree structure is constructed on each PU from the particles involved in its own domain. This tree is called as a local tree, which is not sufficient to assess the force of gravity on particles contained in PU1. Thus we need information from other PUs. After making the local trees, we walk along them in other PUs as a “box” which has the same dimension as the computational domain of PU1. As a result, we find the tree nodes that are not opened when they interact with the particles in PU1 (upper middle panel). These tree nodes data are sent to PU1 as the data of “particles”, since it is not necessary to open the nodes anymore when they are used to calculate the gravitational force on the particles in PU1 (right panel). Finally, we can reconstruct the tree structure, i.e. locally essential tree, from the particles in PU1 plus the “particles” from other PUs (lower middle panel). Utilizing this new tree structure, we can assess the force of gravity on the particles in PU1. We can do the same operation on other PUs simultaneously, therefore, the acceleration on all the particles can be evaluated. The tree structure is also used to obtain the neighbor SPH particle list (see section 2.2), which will also be used in ray tracing routine again (see section 2.3). At present, the code is not designed to utilize GRAPE boards, however, will be upgraded to a parallel-GRAPE-Tree code.

2.2. Hydrodynamics

Hydrodynamics is calculated by SPH scheme, based upon the method summarized in Thacker et al. (2000). The local density of the gas is evaluated by following standard convolution method:

$$\rho(\mathbf{x}_j) = \sum_i m_i W(|\mathbf{x}_i - \mathbf{x}_j|, h_{ij}) \quad (1)$$

where

$$h_{ij} = (h_i + h_j)/2, \quad W(|\mathbf{x}|, h) = \frac{W_s(|\mathbf{x}|/h)}{h^3}$$

and

¹ <http://grape.astron.s.u-tokyo.ac.jp/makino/software/>

$$W_s(y) = \frac{1}{4\pi} \begin{cases} 4 - 6y^2 + 3y^3, & 0 \leq y \leq 1 \\ (2 - y)^3, & 1 < y \leq 2 \\ 0, & y > 2. \end{cases} \quad (2)$$

The equation of motion for each SPH particle is given by

$$\frac{d\mathbf{v}_i}{dt} = \mathbf{g}_i - \sum_j m_j \left(\frac{P_i}{\rho_i^2} + \frac{P_j}{\rho_j^2} + \Pi_{ij} \right) \times \nabla_i [W(|\mathbf{x}_i - \mathbf{x}_j|, h_i) + W(|\mathbf{x}_i - \mathbf{x}_j|, h_j)] / 2. \quad (3)$$

Here \mathbf{g}_i is the gravitational acceleration and Π_{ij} denotes the standard 'Monaghan' artificial viscosity (Monaghan 1992),

$$\Pi_{ij} = \frac{-\mu_{ij}(c_i + c_j)/2 + 2\mu_{ij}^2}{(\rho_i + \rho_j)/2}, \quad (4)$$

where,

$$\mu_{ij} = \begin{cases} h_{ij} \mathbf{v}_{ij} \cdot \mathbf{x}_{ij} / (|\mathbf{x}_i - \mathbf{x}_j|^2 + 0.01h_{ij}^2), & \mathbf{v}_{ij} \cdot \mathbf{x}_{ij} < 0 \\ 0, & \mathbf{v}_{ij} \cdot \mathbf{x}_{ij} \geq 0 \end{cases} \quad (5)$$

The equation of motion is integrated by the standard leap-frog method. We also employ the update scheme of SPH smoothing radius h_i given in equations (10) and (11) in Thacker et al. (2000), which adjust the number of neighbor particles to nearly constant. We set the number of neighbors to be 100 in our simulations. We also remark that we use the tree structure in order to obtain the neighbor list.

In order to parallelize SPH scheme, parallelization of neighbor search algorithm is inevitable and crucial. The method to parallelize neighbor search algorithm is schematically shown in Figure 2. Suppose we have four PUs and try to find the neighbor list of the particles in PU1. Left panel shows the first phase of the algorithm, in which local tree is made on each PU. Since the neighbor particles would be included in other PUs, local tree is not enough to find the complete list of neighbors. In order to obtain the information from other PUs, the particles in the "margin" of PU1 are found by using the local trees in other PUs. The obtained data of particles are sent to PU1 (upper middle panel). The "margins" surrounding the boundary of the domain associated with PU1, are determined by the maximal radius among the particles in PU1. The radius is two times the maximal smoothing radius (denoted as $2h_{\max}(\text{PU1})$ in the upper middle panel). Finally, the list of particles which might be in the neighbor of particles in PU1 is completed (right panel). Using this list, locally essential tree is reconstructed, which is used to find neighbor particles in PU1 (lower left panel). We can perform same operations on other PUs simultaneously, hence we obtain the complete list of neighbor particles for all particles.

2.3. Ray Tracing

It would be possible to solve full three dimensional radiation hydrodynamic problem in the next decade, but it is not possible at present. Actually, Nakamoto, Umemura, & Susa (2001) have performed fully three dimensional simulation of radiation transfer for ionizing photons including the effects of diffuse radiation. However, the computational cost was so expensive that it cannot be used directly for the radiation hydrodynamic problems.

In our code, so called on-the-spot approximation (Spitzer 1978) is employed. We solve the transfer of ionizing photons directly from the source, whereas we do not solve the transfer of diffuse photons. Instead, it is assumed that the recombination photons are absorbed in the very neighbour of the spatial position where they are emitted. Thus, the radiation transfer equation for intensity I_ν at frequency ν reduces to a very simple equation:

$$\frac{dI_\nu}{dr} = -n_{\text{HI}}\sigma_\nu I_\nu, \quad (6)$$

where the re-emission term is not included, since it is taken into account in the reduced recombination rate. This transfer equation (6) itself is easily integrated to find $I_\nu \propto \exp(-\tau_\nu)$, where the optical depth τ_ν is defined as:

$$\tau_\nu \equiv \int_0^r n_{\text{HI}}\sigma_\nu dr,$$

where r is the distance from the source, n_{HI} is the HI density, and σ_ν denotes the photoionization cross section. The on-the-spot approximation reduces the computational cost drastically, if the number of the sources is much smaller than the number of SPH particles. We also note that the frequency dependence of optical depth is originated from σ_ν , which dependence is already known. Therefore, all we need is the optical depth at a certain frequency from in order to assess the optical depth at arbitrary frequency.

It is not trivial to assess the optical depth in SPH scheme. Kessel-Deynet & Burkert (2000) have proposed a scheme for SPH, which utilize the neighbour lists of SPH particles to create grid points on the rays from the source

to SPH particles. In fact, we have parallelized the scheme to use in our previous numerical simulations on the photoevaporation of proto-dwarf galaxies (Susa & Umemura 2004a; Susa & Umemura 2004b). However, in case the number of SPH particles are very large, computational cost of grid points creation on the light ray is not negligible. Moreover, the parallelized version of the code cannot be applied to the problems including multiple sources. Thus, we use the similar method which is slightly different from the original Kessel-Deynet's scheme.

In our new scheme, we do not create so many grid points on the light ray. Instead, we just create one grid point per one SPH particle in its neighbor. The method is described schematically in Figure 3. Suppose that we are trying to assess the optical depth of the particle “0” from two sources “S1” ($\tau_{0\leftarrow S1}$) and “S2” ($\tau_{0\leftarrow S2}$). As the first step, we make a thorough search on the neighbor list of the particle “0” to find the “upstream” particles which are closest to the light rays. The “upstream” particles are found by a simple criterion, that the angles θ_1 and θ_2 are the smallest. In the case of Figure 3, particles “4” and “2” are chosen as the “upstream” particles.

Next, we create the grids on the rays. The grid points on the rays are found as the intersections (marked as wedge-shapes in the figure) of the light rays and the sphere with the radius which equals to the distance between the sources and the “upstream” particles. The physical variables on the particles are mapped onto the intersection points from the “upstream” particles. Using the mapped quantities, the differential optical depths between the intersections and particle “0” ($\Delta\tau_{0\leftarrow S1}$ and $\Delta\tau_{0\leftarrow S2}$) are evaluated by simple trapezium formula. Finally, we obtain the optical depths as

$$\tau_{0\leftarrow S1} = \tau_{4\leftarrow S1} + \Delta\tau_{0\leftarrow S1} \quad (7)$$

$$\tau_{0\leftarrow S2} = \tau_{2\leftarrow S2} + \Delta\tau_{0\leftarrow S2} \quad (8)$$

where $\tau_{4\leftarrow S1}$ and $\tau_{2\leftarrow S2}$ denote the optical depth from S1 to particle 4 and the one from S2 to particle 2. Clearly, we need the optical depth of particles 4 and 2 before we assess $\tau_{0\leftarrow S1}$ and $\tau_{0\leftarrow S2}$. Therefore, we have to evaluate the optical depth of all particles in reverse order of the distance from the source.

If we try to parallelize the code, we need communications of optical depth between the processors, since we have to assess the optical depth of each particles in order in the computational domain decomposed by ORB (see section 2.1). Consequently, we have to wait to assess the optical depth until the information from “upstream” processors arrive. Because of this waiting time, the parallelization efficiency becomes very poor.

In order to overcome this problem, we incorporate two tricks. First, we use Multiple Wave Front (MWF) technique which was originally developed by Nakamoto, Umemura, & Susa (2001). Following their method, we can overlap the calculations of optical depth for multiple sources. Since the number of “waiting” processors is reduced for multiple sources, the parallelization efficiency becomes the better the number of sources gets larger. Second, we use the scheme proposed by Hieneman et al. (2005), which accelerates MWF for small number of sources. In their method, processors have to wait only while the “upstream” processors are calculating the optical depth of particles on the boundary of computational domain (See Figure 4). Therefore, the “waiting” time is greatly reduced, which also helps to improve the parallelization efficiency.

Figure 4 shows an example of propagation of transactions in computational domains. Suppose we have two sources (denoted by two stars) and four PUs. Each panel shows a step of transaction, which is composed of calculations and communications. In the shaded area, the optical depths of SPH particles are calculated, and the arrows between the rectangles show the required communications. We have 5 steps in this example, which guarantees that the information from upstream PUs have arrived before the calculations of optical depths in its own processor. The PUs marked by numbers 1 and/or 2 denote the one in which the calculation for sources 1 and/or 2 have finished. In the first panel, all four PUs are calculating the optical depth for both of the sources simultaneously, assuming the optical depths at the boundary particles are zero. The parallelization efficiency is very close to unity in this first step. In the second panel, the calculated optical depths are sent to the neighbor downstream PUs. In the third panel, the optical depths at the opposite side of the boundary are assessed by just summing up the received optical depths at the boundary and the optical depths calculated at the first step in the attached PUs. The calculated boundary data are sent to the downstream again (fourth panel). After receiving all the required data at the boundary, the optical depths in the inner part are calculated by the sum of the received boundary value and the optical depth evaluated at the first step.

Here we have to remark that this parallelization scheme could introduce very slight difference among the numerical results of various number of processors. In the above scheme, we have to give orders among the processors, otherwise we cannot define the “upstream” or “downstream” processors. This means when we search the “upstream particle” for an SPH particle, one cannot choose the particles located in “downstream” processors. Consequently, especially in case both of the source and the SPH particle under consideration are located near the boundary of the processors, such ordering constraint could give different choice of the “upstream” particle from the one obtained in serial calculation, since there are no such additional constraints for the serial case. Thus the numerical results obtained from different number of processors are not exactly the same.

2.4. Chemical Reactions and Energy Equations

The non-equilibrium chemistry and radiative cooling for primordial gas are calculated by the code developed by Susa & Kitayama (2000), in which H_2 cooling and reaction rates are taken from Galli & Palla (1998). Atomic cooling by hydrogen is also taken into account, utilizing the fitting formula given in Fukugita & Kawasaki (1994). Helium is not included in our code at present, but it will be in the near future (see Appendix 1). Since we are primarily interested in the formation of first objects and their feedback processes, we neglect the cooling by metals and dusts in the present code. We take into consideration the chemistry for H , H^+ , H^- , H_2 , H_2^+ and e^- .

The photoionization rate of HI and the photoheating rate for each SPH particle labelled as i are respectively given by

$$k_{\text{ion}}^{(1)}(i) = n_{\text{HI}}(i) \int_{\nu_L}^{\infty} \int \frac{I_{\nu}(i)}{h\nu} \sigma_{\nu} d\Omega d\nu, \quad (9)$$

$$\Gamma_{\text{ion}}^{(1)}(i) = n_{\text{HI}}(i) \int_{\nu_L}^{\infty} \int \frac{I_{\nu}(i)}{h\nu} \sigma_{\nu} (h\nu - h\nu_L) d\Omega d\nu. \quad (10)$$

Here $n_{\text{HI}}(i)$ represents the number density of neutral hydrogen at i -th particle, σ_{ν} is the photoionization cross section, which is taken from the table in Shapiro & Kang (1987). The frequency at the Lyman limit is denoted by ν_L , and Ω is the solid angle. $I_{\nu}(i)$ is the intensity of the ultraviolet radiation that irradiate i -th particle, which is obtained by the scheme described in section 2.3. Remark that the equations (9) and (10) denote the general formulae of those rates at arbitrary spatial position, omitting the suffix i .

In case the optical depth for ionizing photon for a single SPH particle is moderate, the equations (9) and (10) are valid. If the optical depth becomes much larger than unity, however, those expressions could lead to essentially zero ionization and heating rates because the equations do not conserve the number of photons numerically. Thus, we need something like photon conserving method (Kessel-Deynet & Burkert 2000; Abel, Norman & Madau 1999) in order to avoid this difficulty.

For the purpose to find better formulae for optically thick regime, we combine equations (9),(10) without the suffix i and (6) to rewrite the ionization rate and the photoheating rate as follows:

$$k_{\text{ion}} = -\frac{1}{4\pi r^2} \frac{d}{dr} \int_{\nu_L}^{\infty} \frac{L_{\nu}^* \exp(-\tau_{\nu})}{h\nu} d\nu, \quad (11)$$

$$\Gamma_{\text{ion}} = -\frac{1}{4\pi r^2} \frac{d}{dr} \int_{\nu_L}^{\infty} \frac{L_{\nu}^* \exp(-\tau_{\nu})}{h\nu} (h\nu - h\nu_L) d\nu, \quad (12)$$

where L_{ν}^* denotes the intrinsic luminosity of the source and r is the distance from the source. Here we also use the formal solution of equation (6) and assume that size of the source is much smaller than r .

Now we are ready to derive the better formula, that are the ‘‘volume averaged’’ rates:

$$\begin{aligned} k_{\text{ion}}^{(2)}(i) &\equiv \overline{k_{\text{ion}}} = \frac{\int_{r_i - \Delta r_i/2}^{r_i + \Delta r_i/2} k_{\text{ion}} r^2 dr}{\int_{r_i - \Delta r_i/2}^{r_i + \Delta r_i/2} r^2 dr}, \\ &= \frac{3}{\Delta r_i} \frac{\Phi_1(r_i - \Delta r_i/2) - \Phi_1(r_i + \Delta r_i/2)}{3r_i^2 + \Delta r_i^2/4}, \end{aligned} \quad (13)$$

$$\begin{aligned} \Gamma_{\text{ion}}^{(2)}(i) &\equiv \overline{\Gamma_{\text{ion}}} = \frac{\int_{r_i - \Delta r_i/2}^{r_i + \Delta r_i/2} \Gamma_{\text{ion}} r^2 dr}{\int_{r_i - \Delta r_i/2}^{r_i + \Delta r_i/2} r^2 dr}, \\ &= \frac{3}{\Delta r_i} \frac{\Phi_2(r_i - \Delta r_i/2) - \Phi_2(r_i + \Delta r_i/2)}{3r_i^2 + \Delta r_i^2/4}, \end{aligned} \quad (14)$$

where

$$\Phi_1(r) = \int_{\nu_L}^{\infty} \frac{L_{\nu}^* \exp(-\tau_{\nu})}{4\pi h\nu} d\nu, \quad (15)$$

$$\Phi_2(r) = \int_{\nu_L}^{\infty} \frac{L_{\nu}^* \exp(-\tau_{\nu})}{4\pi h\nu} (h\nu - h\nu_L) d\nu. \quad (16)$$

Here r_i is the distance between the source and i -th particle, Δr_i denotes the spatial step of ray tracing integration, which satisfy

$$r_j = r_i - \Delta r_i / 2, \quad (17)$$

where j denotes the label of the particle located at ‘‘upstream’’ of i -th particle, which is found by the algorithm described in section 2.3.

The above formula has an important advantage that the propagation of ionization front is properly traced even for a large particle separation with optical depth greater than unity. However, in the neighbor of the source, equations (9) and (10) might give better value than equations (13) and (14) do because of the poor spatial resolution and high ionization degree. Thus, we employ following formula for ionization and photoheating rates, in which the rates are switched to one another depending on the local optical depth:

$$k_{\text{ion}}(i) = \frac{k_{\text{ion}}^{(1)}(i)}{1 + \Delta\tau_i / \Delta\tau_{\text{cr}}} + \frac{\Delta\tau_i / \Delta\tau_{\text{cr}} k_{\text{ion}}^{(2)}(i)}{1 + \Delta\tau_i / \Delta\tau_{\text{cr}}}, \quad (18)$$

$$\Gamma_{\text{ion}}(i) = \frac{\Gamma_{\text{ion}}^{(1)}(i)}{1 + \Delta\tau_i / \Delta\tau_{\text{cr}}} + \frac{\Delta\tau_i / \Delta\tau_{\text{cr}} \Gamma_{\text{ion}}^{(2)}(i)}{1 + \Delta\tau_i / \Delta\tau_{\text{cr}}}. \quad (19)$$

Here $\Delta\tau_{\text{cr}}$ is a constant at which the switching occurs, that is 10^{-3} in our simulations. $\Delta\tau_i$ is the local optical depth defined as:

$$\Delta\tau_i \equiv \frac{1}{2} (n_{\text{HI}}(j) + n_{\text{HI}}(i)) \sigma_{\nu_L} \Delta r_i.$$

We also remark that the integral in frequency space in equations (15) and (16) can be performed in advance of the simulations. As a result, Φ_1 and Φ_2 are found to be the functions of the optical depth only at the Lyman limit, since we already know the frequency dependence of the cross section τ_ν , which is proportional to σ_ν . Therefore we can create tables of Φ_1 and Φ_2 as functions of τ_{ν_L} , or we have analytic formula for some particular cases (Susa & Umemura 2000; Susa & Kitayama 2000; Nakamoto, Umemura, & Susa 2001). Consequently, we need that optical depth just at the Lyman-limit by ray tracing. We also note that this formulation for pure hydrogen gas can be extended to the hydrogen + helium gas (Appendix 1), although it has not been implemented yet.

The H_2 photodissociation rate is also evaluated by similar method. In order to assess the photodissociation rate, the transfer equation of Lyman-Werner(LW) radiation is necessary. However, the frequency dependent line transfer of LW band takes too much computational cost. Thus, we assume the ‘‘self-shielding function’’ derived by Draine & Bertoldi (1996), which gives the photodissociation rate of H_2 as

$$k_{\text{dis}}^{(1)} = k_{\text{dis}}^{(0)} \left(\frac{r_0}{r} \right)^2 f_{\text{sh}} \left(\frac{N_{\text{H}_2}}{10^{14} \text{cm}^{-2}} \right) \quad (20)$$

where

$$f_{\text{sh}}(x) = \begin{cases} 1, & x \leq 1 \\ x^{-3/4}, & x > 1 \end{cases}$$

Here N_{H_2} is the column density of hydrogen molecules measured from the source star, $k_{\text{dis}}^{(0)}$ is the unshielded photodissociation rate in the neighbor of the source at $r = r_0$. We also multiply the geometrical dimming factor, $(r_0/r)^2$. The simplest method is to use equation (20) directly, which works well in the case $\Delta N_{\text{H}_2} \lesssim 10^{14} \text{cm}^{-2}$ is satisfied. Here ΔN_{H_2} denotes the H_2 column density of a single spatial grid generated along the light ray, i.e. $\Delta N_{\text{H}_2} = \frac{1}{2} (n_{\text{H}_2}(j) + n_{\text{H}_2}(i)) \Delta r_i$.

However, for $\Delta N_{\text{H}_2} \gg 10^{14} \text{cm}^{-2}$, the photodissociation rate is significantly reduced by the absorption in LW band while LW photons are passing through only a single grid. This could delay the propagation of H_2 dissociation front because the significant amount of dissociation photons are absorbed in a single grid without being used to dissociate H_2 . In order to overcome this problem, we take similar approach to that in photoionization problem. In the case of photoionization, we use a sort of ‘‘photon conserving’’ method by integrating the photoionization rate over a single grid. Similarly, we integrate the photodissociation rate over a single grid, and assess the volume averaged photodissociation rate as follows:

$$\begin{aligned} k_{\text{dis}}^{(2)}(i) &\equiv \overline{k_{\text{dis}}} = \frac{\int_{r_i - \Delta r_i / 2}^{r_i + \Delta r_i / 2} k_{\text{dis}} r^2 dr}{\int_{r_i - \Delta r_i / 2}^{r_i + \Delta r_i / 2} r^2 dr} \\ &= \frac{r_0^2}{r_i^2 + \frac{\Delta r_i^2}{12}} \frac{k_{\text{dis}}^{(0)}}{\Delta r_i n_{\text{H}_2}(i)} \int_{N_{\text{H}_2}^-}^{N_{\text{H}_2}^+} f_{\text{sh}} \left(\frac{N_{\text{H}_2}}{10^{14} \text{cm}^{-2}} \right) dN_{\text{H}_2} \end{aligned} \quad (21)$$

where $N_{\text{H}_2}^{\pm}$ denote the H_2 column density at $r_i \pm \Delta r_i/2$, respectively. Note that the factor $k_{\text{dis}}^{(0)}/n_{\text{H}_2}$ can be factorized outside the integral since $k_{\text{dis}}^{(0)}$ is proportional to n_{H_2} . The last integral in the above equation is easily performed analytically. Thus, we obtain the expression of volume averaged photodissociation rate in our scheme. Following the method in the case of photoionization, we also employ the switching scheme from/to the optically thin to/from optically thick regime described in equation (19) (switches from/to expression in equation (20) to/from equation (21)).

Now we are ready to integrate the rate equations and energy equations implicitly:

$$y_i^{(n+1)} = y_i^{(n)} + k_i^{(n+1)} \Delta t, \quad (22)$$

$$\epsilon^{(n+1)} = \epsilon^{(n)} + \left(\Gamma^{(n+1)} - \Lambda^{(n+1)} \right) \Delta t + \Delta t \left[\frac{d\epsilon}{dt} \right]_{\text{ad}}^{(n)}. \quad (23)$$

where

$$\left[\frac{d\epsilon}{dt} \right]_{\text{ad}}^{(n)} = \sum_j m_j \left(\frac{P_i}{\rho_i^2} + \frac{1}{2} \Pi_{ij} \right) (\mathbf{v}_i - \mathbf{v}_j) \nabla_i W(|\mathbf{x}_i - \mathbf{x}_j|, h_{ij}) \quad (24)$$

Here the suffix on the right shoulders of the characters denote the labels of the grid in time coordinate. Δt is the time step, which is given by the algorithm discussed in section 2.5. y_i and ϵ represent the i -th chemical species and internal energy of the gas. k_i , Γ and Λ denote the reaction rate of i -th species, photoheating rate, and cooling rate, all of which are assessed at $(n+1)$ -th time step, while the last term in the second equation denotes the adiabatic term, which is evaluated at n -th time step. In other words, only the adiabatic term is taken into account in an explicit form. Using these equations, we find the solutions $\{y_i^{(n+1)}\}$ and $\epsilon^{(n+1)}$ for all particles by iterative operations.

2.5. Time Step Control

It is possible to use individual time step control depending on the local density in hydrodynamic simulations. However, in radiation hydrodynamic simulations, the justification of the scheme is unknown and uncertain since the effects of radiation field is quite global. Therefore, we use synchronous time steps for all particles.

As a first step, Δt is set as the minimal value among the Courant conditions and the time scales of accelerations for all SPH particles:

$$\Delta t_{\text{hydro}} = \min \left[\frac{h_i}{\max(c_{si}, v_i)}, \sqrt{\frac{h_i}{\dot{v}_i}} \right] \quad \text{for all } i. \quad (25)$$

Afterwards, we try to find solutions of the rate equations and energy equations for all particles by the implicit time integration solver. If we fail to find the solutions, i.e. the convergence is very slow, then we divide the time step by two, and try to find the solutions again. We continue this operation until we find the solutions within reasonable iteration steps (nominally 20). After finding the solution for energy equations and chemical reaction equations, we update the particle positions and velocity by explicit leap-frog time integration.

3. Results of Test Calculations

We perform various tests with the code, and will show the results comparing with the numerical solutions from one dimensional radiation hydrodynamic simulations. We use 8 nodes (16 Xeon processors with gigabit ethernet) and 1048576 SPH particles for the tests unless stated.

3.1. Expanding HII Region in Uniform Media

In this test, we put a single source at the center of the uniform gas cloud and trace the propagation of ionization front. The initial number density of the gas is $n_{\text{H}} = 0.01 \text{cm}^{-3}$, and the temperature is $T = 3 \times 10^2 \text{K}$. The ionizing photon luminosity of the source is $S = 1.33 \times 10^{50} \text{s}^{-1}$ and the spectrum is black body with $T_* = 9.92 \times 10^4 \text{K}$, that are the parameters of POPIII stars with $120 M_{\odot}$ (Baraffe, Heger & Woosley 2001).

Figure 5 shows the propagation of ionization front (r_{I}). Numerical results from the code are shown by red dots, whereas the dotted line denotes the results from the one dimensional Piecewise Parabolic Method (PPM) code (Colella & Woodward 1984). The results agree well with each other. Note that 1D-PPM code is also tested by the comparison with analytic solutions and results from the similar code developed by Tetsu Kitayama (Kitayama et al. 2004), and the two results agree very well with each other.

Figure 6 shows the spatial distributions of physical quantities (HI fraction, temperature, density, H_2 fraction) at different snapshots ($t = 10^7 \text{yr}, 10^8 \text{yr}, 10^9 \text{yr}$). The results are also compared with the plots of one dimensional simulation. Slight scatter and deviation is found in the spatial distribution, especially at later epoch. However, the agreement between the two results are acceptable.

3.2. Expanding HII Region in $\rho \propto r^{-2}$ Density Profile

In this test, density distribution is different from the previous test. We assume “core-envelope” structure, where the uniform central core density $n_{\text{H}} = 100\text{cm}^{-3}$ whose radius is 10pc. We also assume the density of the outer envelope that decline as $\propto r^{-2}$, which is typical of the slope in collapsing prestellar gas cloud. Since the Strömgen radius in the core is slightly smaller than the core radius, initial R-type ionization front is stopped in the core. Afterwards, the ionization front changes to D-type. While the D-type front propagating in the envelope, the front type becomes R-type again, because the the slope is steeper than the critical case where $\rho \propto r^{-1.5}$ (Franco, Tenorio-Tagle & Bodenheimer 1990).

The results are compared with the 1-D results again in Figures.7 and 8. Three different lines shown in Figure 8 correspond to $t = 4 \times 10^5\text{yr}, 10^6\text{yr}, 4 \times 10^6\text{yr}$, respectively. At the final epoch, the type of the ionization front is being changed to R-type from D-type. Again, we find good agreement between the two results, although we have slight difference at the final output. At the final epoch, the propagation of the shock front is slightly delayed, which might be caused by the error in evaluating the optical depth in front of the density peak. In fact, the width of the density peak at the D-front is broader than that of the 1D result. Consequently, the ionized region could be slightly smaller in SPH simulation, which can introduce the delay of propagation time of the shock front.

3.3. Expanding HII Region with Multiple Sources

We also show the HI and density structures that are created by multiple sources. We perform RHD simulations with randomly distributed ten sources in the uniform spherical cloud ($n_{\text{H}} = 1\text{cm}^{-3}$, $R=1$ kpc). All of the sources are assumed to have the same effective temperature and the luminosity as in the previous test. The number of particles used in this simulation is half of the previous two tests, i.e. $N_{\text{SPH}} = 524288$.

The panels in Figure 9 show the time evolution of the density (left column) and HI fraction (right column) distributions on a certain spatial slice of the cubic region that are hollowed out from the spherical simulated cloud.

In the first phase, all HII regions expand as R-type and and they reach Strömgen radius (from top panels to middle panels). Afterwards, the photoheated gas starts to expand dynamically, and dense shells are formed surrounding the sources. The shells collide with each other, and web of dense shells is formed (bottom panels). We use this calculation as the benchmark of our code in the next section.

3.4. Speedup by parallelization

We assess the speedup of parallelization by performing simulations with multiple sources in uniform media described in section 3.3. The initial setup of the simulations are the same as in section 3.3. We use 2, 4, 8, 16 and 32 processors (1, 2, 4, 8 and 16 nodes) for the same setup, and compare the clock time per single time step with each other.

We use the first model of FIRST cluster (consists of 16 nodes with 32 processors) in University of Tsukuba for these test runs. The newly being developed PC cluster “FIRST” is designed to elucidate the origin of first generation objects in the Universe through large-scale simulations. The cluster will consist of 256 nodes (each node has dual Xeon processors) connected by two dimensional hyper-crossbar quad-gigabit network utilizing trunk technology. The most striking feature of the system is that each node has small GRAPE6 PCI-X board called Brade-GRAPE. The Brade-GRAPE has four GRAPE6 chips per board (thus 1/8 processors of a full board). The board has basically the same function as GRAPE-6A (Fukushige, Makino & Kawai 2005), but it has an advantage that it can be installed in 2U server unit of PC clusters due to the short height of its heat sink.

Figure 10 shows the speedup of the performance. The vertical axis denotes the clock time by single node run (two processors) divided by the time for N_{node} nodes, and the horizontal axis shows the number of nodes. The dotted line represents the case of ideal speedup, and the symbols correspond to the runs with various number of sources ($N_{\text{source}} = 2, 10, 20$).

Some of present results are slightly better than ideal case (e.g. $N_{\text{node}} = 8$, $N_{\text{source}} = 20$ case). The chief reason of this super linearity is the different convergence speed of implicit solver for different number of nodes. The numerical calculations between the runs with different number of nodes are not exactly the same (see section 2.3). Consequently, the number of time steps vary from runs to runs and the convergence speed for each time step is also not identical. Thus, such different convergence property could lead to the super linear speed up. Apart from the fluctuation due to this unevenness of time steps, parallelization efficiency is quite good as far as the number of nodes are smaller than 16 for $N_{\text{source}} \geq 10$.

For $(N_{\text{node}}, N_{\text{source}}) = (16, 2)$ case, the speedup is not as good as those for other runs. This run include only 2 sources, which number is much smaller than the number of nodes. Thus the ‘waiting’ time in the ray tracing routine could emerge. In fact, for larger number of sources, we do not observe such reduction of parallelization efficiency. However, this result also means when we increase the number of nodes to ~ 100 , similar phenomenon is expected with $N_{\text{source}} \sim 10$. Therefore, we have to keep in mind this property when we run the code with much larger number of nodes in the future after the completion of full FIRST cluster.

4. Summary

We have constructed the new code for radiation hydrodynamics designed to be applied to the feedback effects of first generation stars/galaxies. The code can deal with multiple sources, and it can solve the transfer of ionizing photons and photodissociating photons.

The code is already parallelized, and almost ready to be installed in the newly developed full size huge PC cluster ‘‘FIRST’’ in University of Tsukuba. We compare the numerical results with one dimensional calculations, and find the good agreements.

We thank the anonymous referee for important comments. We also thank M. Umemura and T. Nakamoto, K. Ohsuga for careful reading of the manuscript. We thank N. Shibasaki for continuous encouragement. We thank H. Maki for providing the 1D-PPM code. We also thank T. Kitayama for providing the 1-dimensional results, and thank all the collaborators in TSU3 project (<http://www.mpa-garching.mpg.de/tsu3>) for fruitful discussions during the workshop in CITA. The analysis has been made with computational facilities at Center for Computational Science in University of Tsukuba and Rikkyo University. This work was supported in part by Ministry of Education, Culture, Sports, Science, and Technology (MEXT), Grants-in-Aid, Specially Promoted Research 16002003 and Young Scientists (B) 17740110.

Appendix 1. Volume averaged photoionization rate with helium

In this section, we show the basic idea of the volume averaged photoionization/photoheating rate for H/He gas. It could be useful to the readers although we have not implemented yet. First of all, we have the radiation transfer equation assuming the pure absorption (i.e. on-the-spot approximation):

$$\frac{dI_\nu}{dr} = -(n_{\text{HI}}\sigma_\nu^{\text{HI}} + n_{\text{HeI}}\sigma_\nu^{\text{HeI}} + n_{\text{HeII}}\sigma_\nu^{\text{HeII}})I_\nu \quad (\text{A1})$$

where σ_ν^{X} and n_{X} denote the photoionization cross section and number density of X species, respectively. The photoionization rates for HI, HeI and HeII are

$$k_{\text{ion}}^{\text{HI}} = n_{\text{HI}} \int_{\nu_L}^{\infty} \int \frac{I_\nu}{h\nu} \sigma_\nu^{\text{HI}} d\Omega d\nu, \quad (\text{A2})$$

$$k_{\text{ion}}^{\text{HeI}} = n_{\text{HeI}} \int_{\nu_{L\text{HeI}}}^{\infty} \int \frac{I_\nu}{h\nu} \sigma_\nu^{\text{HeI}} d\Omega d\nu, \quad (\text{A3})$$

$$k_{\text{ion}}^{\text{HeII}} = n_{\text{HeII}} \int_{\nu_{L\text{HeII}}}^{\infty} \int \frac{I_\nu}{h\nu} \sigma_\nu^{\text{HeII}} d\Omega d\nu, \quad (\text{A4})$$

Here $\nu_L, \nu_{L\text{HeI}}$ and $\nu_{L\text{HeII}}$ denote the Lyman limit frequency of HI, HeI, HeII respectively.

Combining equation(A1) with equations(A2)-(A4), and perform the integration in solid angle, we have

$$k_{\text{ion}}^{\text{HI}} = -\frac{1}{4\pi r^2} \int_{\nu_L}^{\infty} \frac{n_{\text{HI}}\sigma_\nu^{\text{HI}}}{(n\sigma)_{\text{tot}}} \frac{d}{dr} \frac{L_\nu^* \exp(-\tau_\nu)}{h\nu} d\nu, \quad (\text{A5})$$

$$k_{\text{ion}}^{\text{HeI}} = -\frac{1}{4\pi r^2} \int_{\nu_{L\text{HeI}}}^{\infty} \frac{n_{\text{HeI}}\sigma_\nu^{\text{HeI}}}{(n\sigma)_{\text{tot}}} \frac{d}{dr} \frac{L_\nu^* \exp(-\tau_\nu)}{h\nu} d\nu, \quad (\text{A6})$$

$$k_{\text{ion}}^{\text{HeII}} = -\frac{1}{4\pi r^2} \int_{\nu_{L\text{HeII}}}^{\infty} \frac{n_{\text{HeII}}\sigma_\nu^{\text{HeII}}}{(n\sigma)_{\text{tot}}} \frac{d}{dr} \frac{L_\nu^* \exp(-\tau_\nu)}{h\nu} d\nu, \quad (\text{A7})$$

where

$$(n\sigma)_{\text{tot}} \equiv n_{\text{HI}}\sigma_\nu^{\text{HI}} + n_{\text{HeI}}\sigma_\nu^{\text{HeI}} + n_{\text{HeII}}\sigma_\nu^{\text{HeII}}$$

$$\tau_\nu \equiv \int_0^r (n\sigma)_{\text{tot}} dr$$

Then we assume that the ratio such as $n_{\text{X}}\sigma_\nu^{\text{X}}/(n\sigma)_{\text{tot}}$ in equations (A5)-(A7) are independent of r within the single grid, which is a regular assumption for finite difference scheme. Therefore we can regard the ratio as constants when we integrate the equation within a single grid. The volume averaged rates are as follows:

$$\overline{k_{\text{ion}}^{\text{HI}}} = \frac{3}{\Delta r_i} \frac{\Phi_1^{\text{HI}}(r_i - \Delta r_i/2) - \Phi_1^{\text{HI}}(r_i + \Delta r_i/2)}{3r_i^2 + \Delta r_i^2/4}, \quad (\text{A8})$$

$$\overline{k_{\text{ion}}^{\text{HeI}}} = \frac{3}{\Delta r_i} \frac{\Phi_1^{\text{HeI}}(r_i - \Delta r_i/2) - \Phi_1^{\text{HeI}}(r_i + \Delta r_i/2)}{3r_i^2 + \Delta r_i^2/4}, \quad (\text{A9})$$

$$k_{\text{ion}}^{\text{HeII}} = \frac{3}{\Delta r_i} \frac{\Phi_1^{\text{HeII}}(r_i - \Delta r_i/2) - \Phi_1^{\text{HeII}}(r_i + \Delta r_i/2)}{3r_i^2 + \Delta r_i^2/4}, \quad (\text{A10})$$

where

$$\Phi_1^{\text{HI}}(r) = \int_{\nu_L}^{\infty} \frac{n_{\text{HI}} \sigma_{\nu}^{\text{HI}} L_{\nu}^* \exp(-\tau_{\nu})}{(n\sigma)_{\text{tot}} 4\pi h\nu} d\nu, \quad (\text{A11})$$

$$\Phi_1^{\text{HeI}}(r) = \int_{\nu_{\text{LHeI}}}^{\infty} \frac{n_{\text{HeI}} \sigma_{\nu}^{\text{HeI}} L_{\nu}^* \exp(-\tau_{\nu})}{(n\sigma)_{\text{tot}} 4\pi h\nu} d\nu, \quad (\text{A12})$$

$$\Phi_1^{\text{HeII}}(r) = \int_{\nu_{\text{LHeII}}}^{\infty} \frac{n_{\text{HeII}} \sigma_{\nu}^{\text{HeII}} L_{\nu}^* \exp(-\tau_{\nu})}{(n\sigma)_{\text{tot}} 4\pi h\nu} d\nu. \quad (\text{A13})$$

The photoheating rates are evaluated by exactly the same way as above. The volume averaged photoheating rates are

$$\overline{\Gamma}_{\text{ion}}^{\text{HI}} = \frac{3}{\Delta r_i} \frac{\Phi_2^{\text{HI}}(r_i - \Delta r_i/2) - \Phi_2^{\text{HI}}(r_i + \Delta r_i/2)}{3r_i^2 + \Delta r_i^2/4}, \quad (\text{A14})$$

$$\overline{\Gamma}_{\text{ion}}^{\text{HeI}} = \frac{3}{\Delta r_i} \frac{\Phi_2^{\text{HeI}}(r_i - \Delta r_i/2) - \Phi_2^{\text{HeI}}(r_i + \Delta r_i/2)}{3r_i^2 + \Delta r_i^2/4}, \quad (\text{A15})$$

$$\overline{\Gamma}_{\text{ion}}^{\text{HeII}} = \frac{3}{\Delta r_i} \frac{\Phi_2^{\text{HeII}}(r_i - \Delta r_i/2) - \Phi_2^{\text{HeII}}(r_i + \Delta r_i/2)}{3r_i^2 + \Delta r_i^2/4}, \quad (\text{A16})$$

where

$$\Phi_2^{\text{HI}}(r) = \int_{\nu_L}^{\infty} \frac{n_{\text{HI}} \sigma_{\nu}^{\text{HI}} L_{\nu}^* \exp(-\tau_{\nu})}{(n\sigma)_{\text{tot}} 4\pi h\nu} (h\nu - h\nu_L) d\nu, \quad (\text{A17})$$

$$\Phi_2^{\text{HeI}}(r) = \int_{\nu_{\text{LHeI}}}^{\infty} \frac{n_{\text{HeI}} \sigma_{\nu}^{\text{HeI}} L_{\nu}^* \exp(-\tau_{\nu})}{(n\sigma)_{\text{tot}} 4\pi h\nu} (h\nu - h\nu_{\text{LHeI}}) d\nu, \quad (\text{A18})$$

$$\Phi_2^{\text{HeII}}(r) = \int_{\nu_{\text{LHeII}}}^{\infty} \frac{n_{\text{HeII}} \sigma_{\nu}^{\text{HeII}} L_{\nu}^* \exp(-\tau_{\nu})}{(n\sigma)_{\text{tot}} 4\pi h\nu} (h\nu - h\nu_{\text{LHeII}}) d\nu. \quad (\text{A19})$$

It is also worth to point out that the functions Φ_1^{X} and Φ_2^{X} can be assessed only by the optical depth at three frequencies (ν_L , ν_{LHeI} and ν_{LHeII}), although the expressions (A11) - (A13) and (A17) - (A19) include frequency dependent optical depth τ_{ν} (Nakamoto, Umemura, & Susa 2001). Consequently, we can create the tables of ionization rates and heating rates as functions of optical depth and the ratio $n_{\text{X}} \sigma_{\nu}^{\text{X}} / (n\sigma)_{\text{tot}}$ at Lyman limits (ν_L , ν_{LHeI} and ν_{LHeII}).

References

- Abel, T., Bryan, G. L., & Norman, M. L. 2000, ApJ, 540, 39
 Abel T., Norman M. L., Madau P., 1999, ApJ, 523, 66
 Baraffe, I., Heger, A. & Woosley, S. E. 2001, ApJ, 550, 890
 Barnes, J. & Hut, P., 1986, Nature, 324, 446
 Bromm, V., Coppi, P. S., & Larson, R. B. 1999, ApJ, 527, L5
 Bromm, V., Coppi, P. S., & Larson, R. B. 2002, ApJ, 564, 23
 Colella, P., & Woodward, P.R. 1984, J. Comp. Phys., 1984, 54, 174
 Draine, B. T., & Bertoldi, F. 1996, ApJ, 468, 269
 Dubinski, J. 1996, NewA, 1, 133
 Franco, J., Tenorio-Tagle, G., & Bodenheimer, P. 1990, ApJ, 349, 126
 Fukugita, M. & Kawasaki, M., 1994, MNRAS, 269, 563
 Fukushige, T., Makino, J. & Kawai, A. 2005, astro-ph/0504407
 Galli D. & Palla F. 1998, A&A, 335, 403
 Gnedin, N. Y. & Abel, T., 2001, NewA, 6, 437
 Heinemann, T., Dobler, W., Nordlund, A. & Brandenburg, A., 2005, astro-ph/0503510
 Kessel-Deynet, O. & Burkert, A. 2000, MNRAS, 315, 713
 Kitayama, T., Yoshida, N., Susa, H. & Umemura, M., 2004, ApJ, 613, 631
 Maselli, A., Ferrara, A. & Ciardi, B. 2003, MNRAS, 345, 379
 Mellema, G., Iliev, I. T., Alvarez, M. A. & Shapiro, P.R., 2005, astro-ph/0508416
 Monaghan, J.J. 1992, ARA&A, 30, 543
 Nakamoto, T., Umemura, M., & Susa, H. 2001, MNRAS, 321, 593
 Nakamura F. & Umemura M. 1999, ApJ, 515, 239
 Nakamura, F., & Umemura, M. 2001, ApJ, 548, 19
 Razoumov, A. O., Norman, M. L., Abel, T., & Scott, D. 2002, ApJ, 572, 695
 Rijkhorst, E., Plewa, T., Dubey, A. & Mellema, G. 2005, astro-ph/0505213
 Shapiro, P.R., & Kang, H., 1987, ApJ, 318, 32
 Spitzer, L. Jr. 1978, in Physical Processes in the Interstellar Medium (John Wiley & Sons, Inc. 1978)
 Susa, H. & Kitayama, T. 2000, MNRAS, 317, 175 Prog. Theor. Phys., 100, 63
 Susa, H. & Umemura, M. 2000, ApJ, 537, 578
 Susa, H. & Umemura, M. 2004, ApJ, 600, 1
 Susa, H. & Umemura, M. 2004, ApJ, 610, 5L
 Thacker, J., Tittley, R., Pearce, R., Couchman, P. & Thomas, A. 2000, MNRAS 319, 619
 Yoshida, N., Abel, T., Hernquist, L. & Sugiyama, N., 2003, ApJ, 592, 645

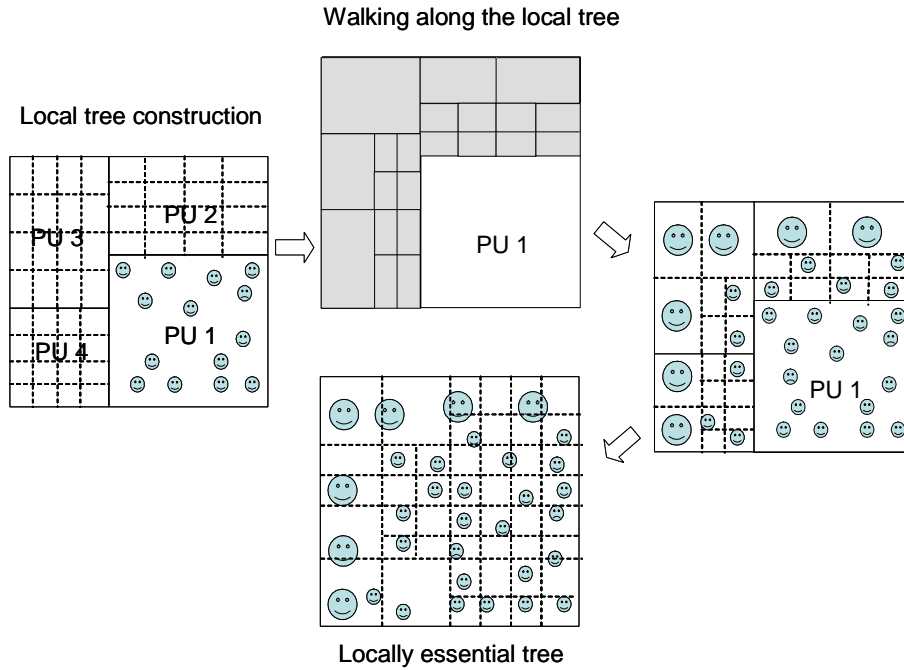


Fig. 1. Parallel tree scheme to assess the force of gravity on the particles included in a processor(PU1) is schematically shown. Left panel shows the initial phase of the algorithm, in which local tree is made on each processor. In the next step, the tree nodes which can interact the particles in PU1 are found by walking along the local tree. The data of the nodes are sent to PU1 as “particles” that do not have inner structure (upper middle panel). Finally, we have the complete list of particles which can interact with the particles in PU1(right panel). Utilizing this particle list, we can assess the force of gravity on the particles in PU1 by building up and walking down the locally essential tree (lower middle).

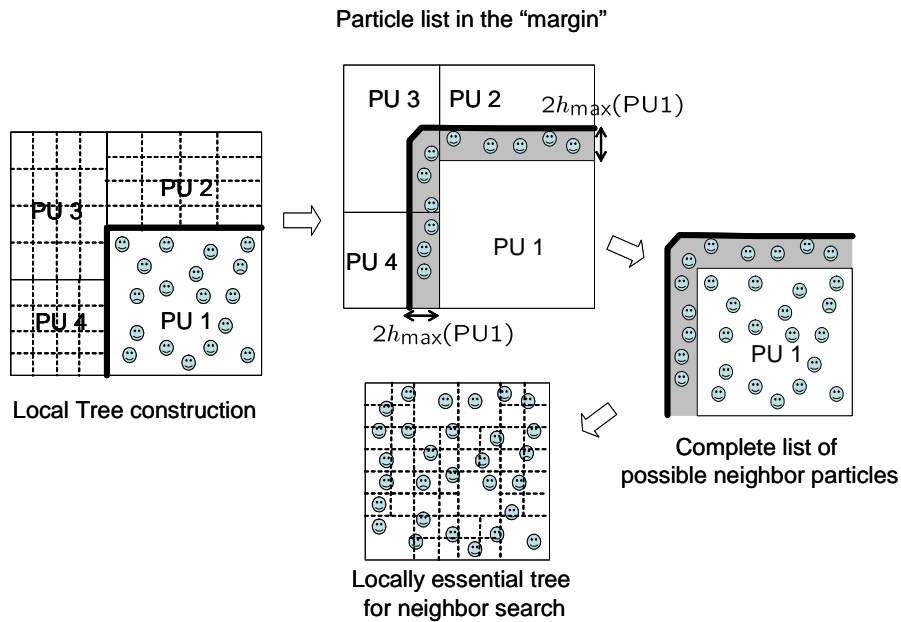


Fig. 2. Employed neighbor search algorithm on parallel computer system to obtain the neighbour list of a certain processor (PU1) is shown. Left panel shows the initial phase of the algorithm, in which local tree is made on each processor. In the next step, the data of particles in the “margin” of PU1 are sent to PU1 (upper middle). Finally, the list of particles which can be in the neighbor of particles in PU1 is completed (right panel). Using this list, locally essential tree is re-constructed, which is used to find neighbor particles in PU1 (lower middle).

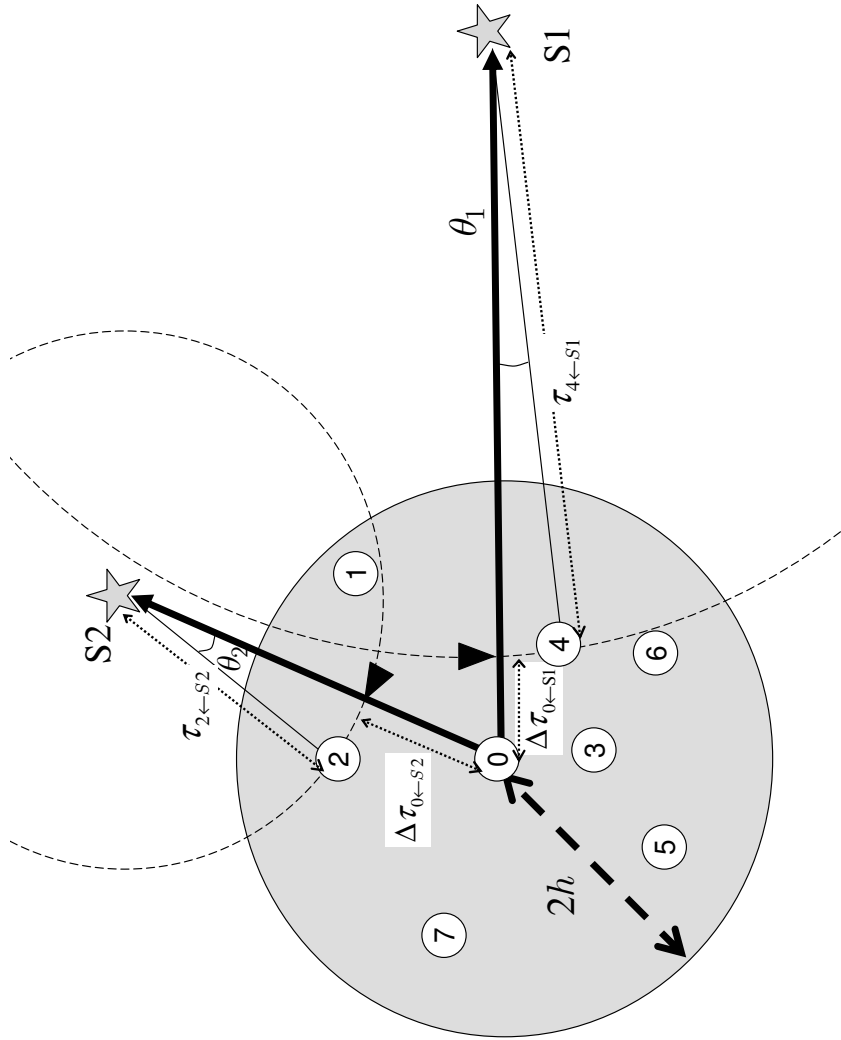


Fig. 3. Ray tracing method for multiple sources are schematically shown. Numbers in circles represent the ID of SPH particles in the neighbor of SPH particle “0”. $S1$ and $S2$ represent the position of two sources. Two wedge-shapes show the position on which the optical depth from the sources are projected from corresponding particles (in this case 2 and 4).

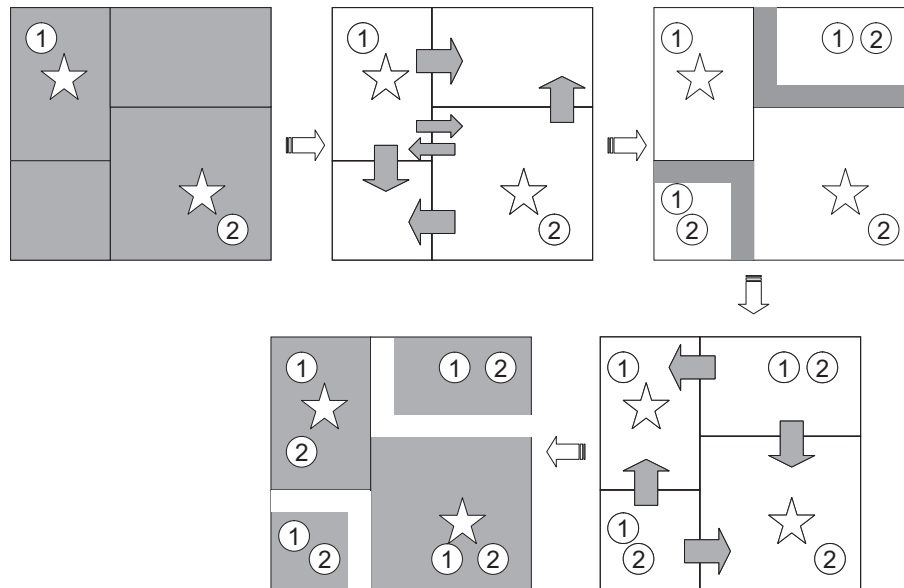


Fig. 4. Order of computations and communications for ray tracing on parallel machine is shown schematically for an example. In this example, the computational domain is decomposed into 2D, and consists of 4 nodes. The calculations and communications proceed along the direction of small open arrows. The position of two sources are shown by star-shaped symbols. The shaded region on the nodes are occupied by computation, and the shaded arrows represents the direction of the present communications.

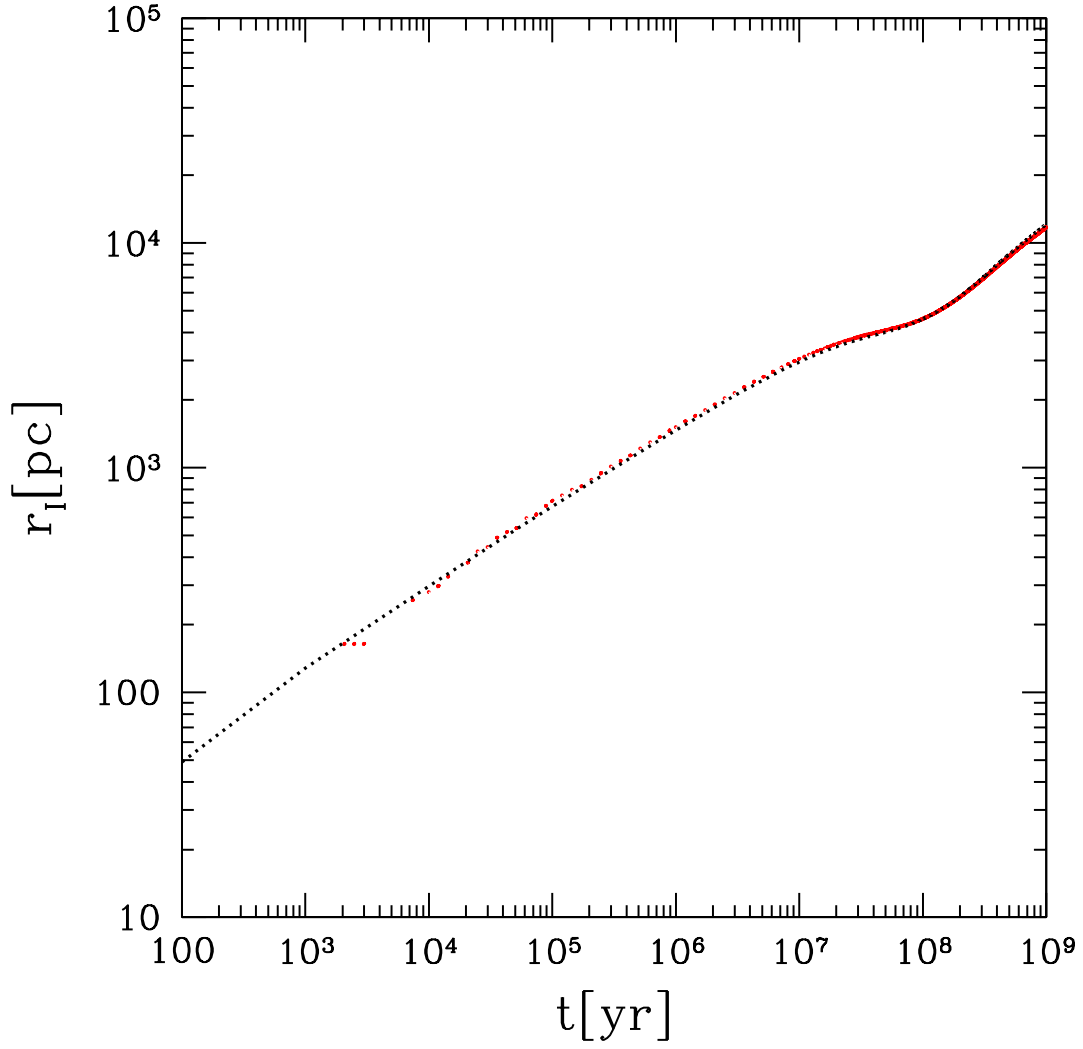


Fig. 5. Propagation of ionization front in uniform media is shown. Initial density and temperature is $n_{\text{H}} = 0.01 \text{cm}^{-3}$, $T = 3 \times 10^2 \text{K}$. The ionizing photon luminosity of the source is $S = 1.33 \times 10^{50} \text{s}^{-1}$ and the spectrum is black body with $T_* = 9.92 \times 10^4 \text{K}$. Horizontal axis shows the time after the ignition of central star, and the vertical axis shows the position of ionization front, defined as the radius at which the fraction of HI is 0.5. Red dots denote the results from the SPH code, whereas the dotted line denotes the ionization front position from the 1D simulation.

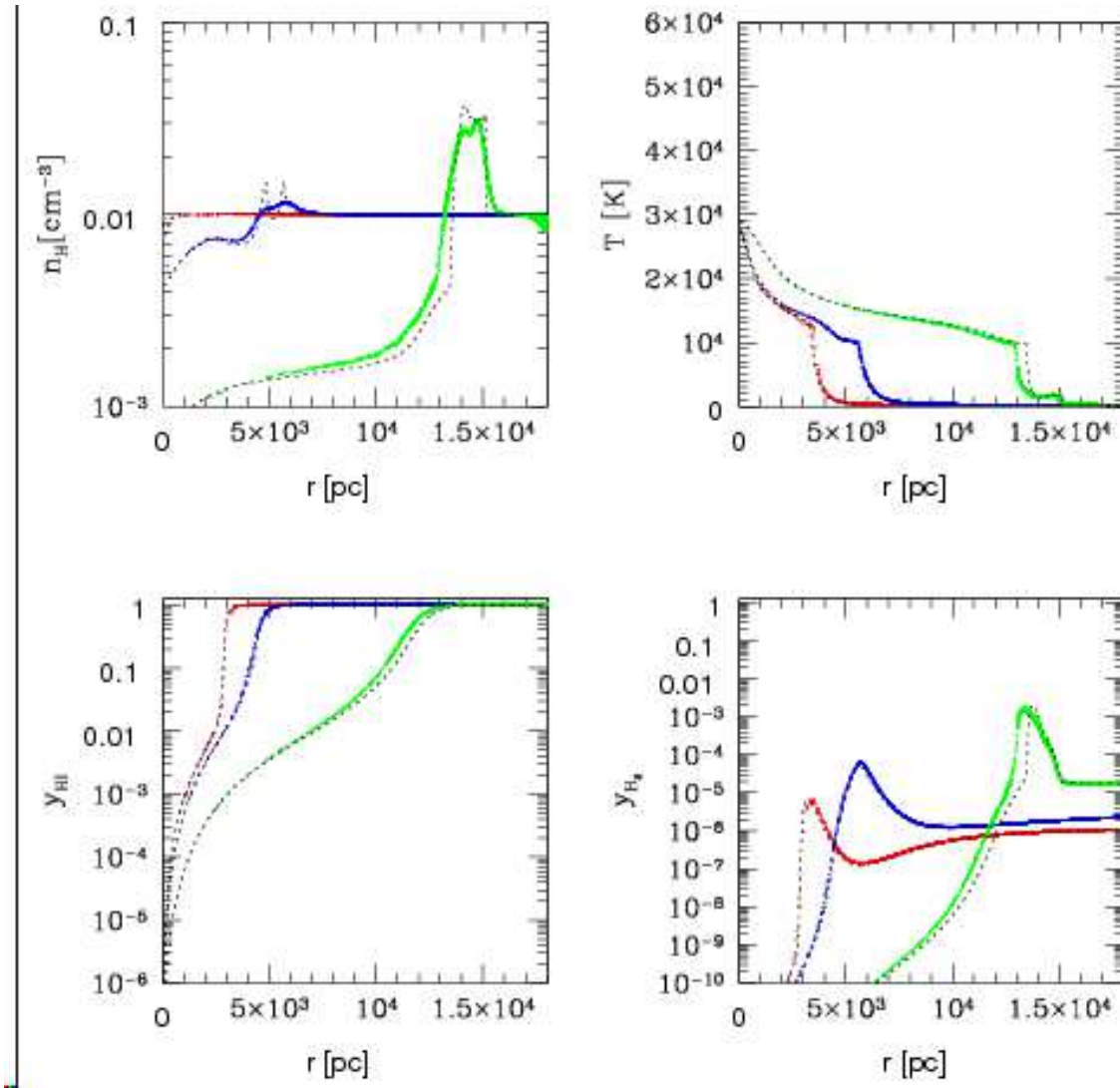


Fig. 6. Spatial distribution of physical quantities at three time snapshots ($t = 10^7, 10^8, 10^9$ yr) are shown for the run shown in Fig.5. Upper panels show the density and temperature, and the lower panels show the HI fraction and H₂ fraction. Horizontal axes denote the distance from the source. The dotted lines denote the results from the 1D simulation.

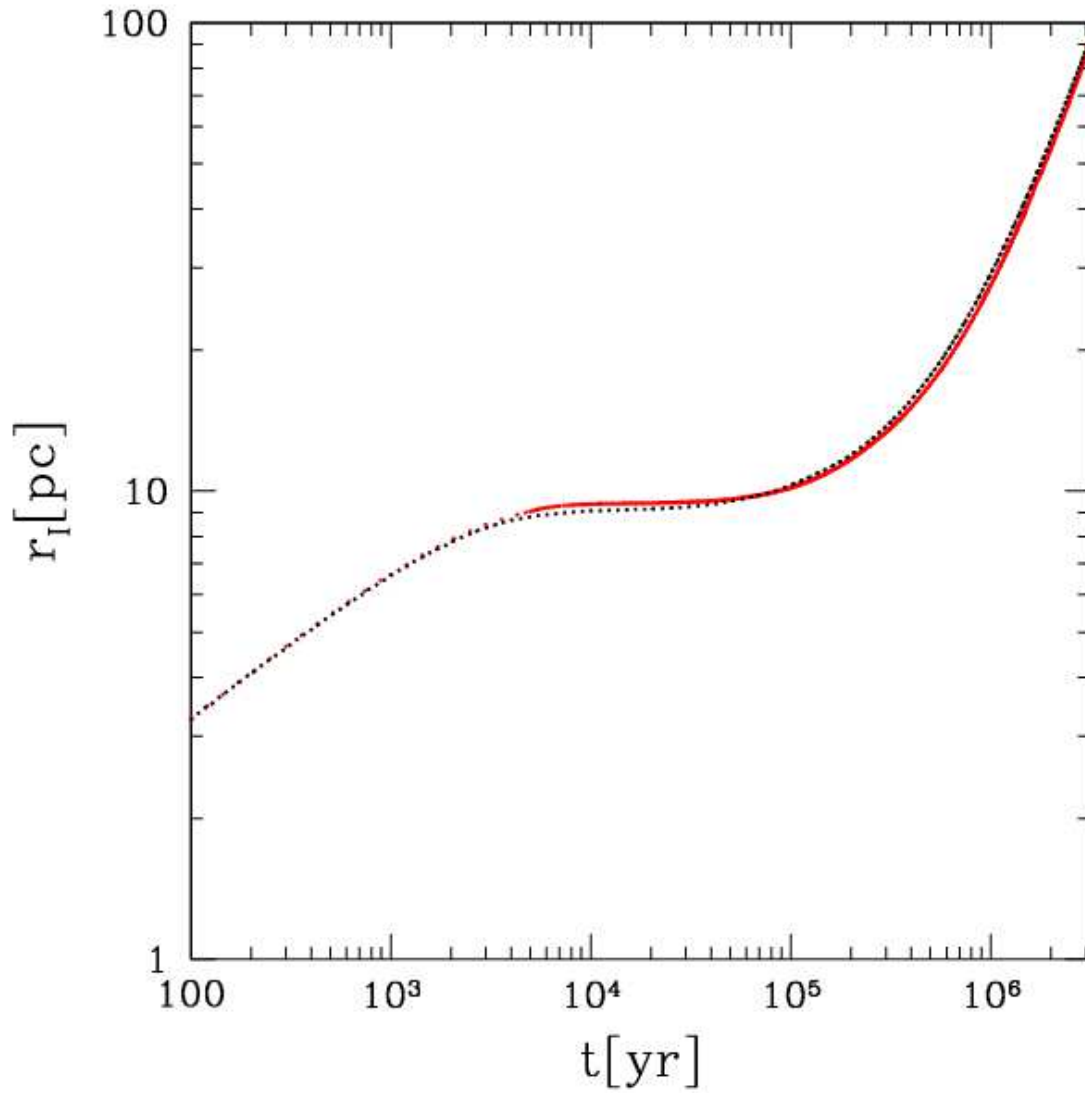


Fig. 7. Same as Fig.5, except that the initial density distribution is core-envelope structure, discussed in section3.2.

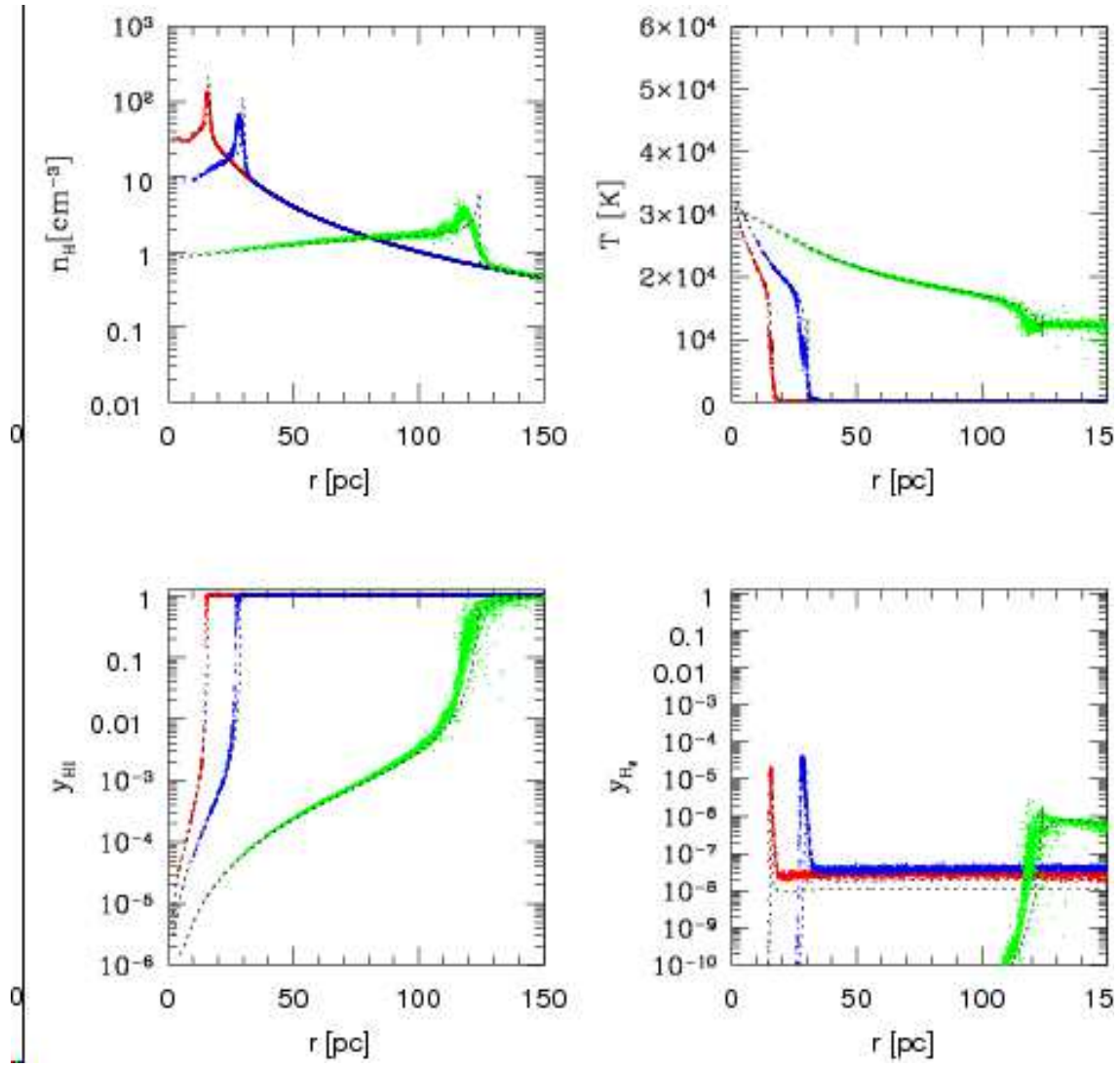


Fig. 8. Same as Fig.6, except that the initial density distribution is core-envelope structure, discussed in section 3.2

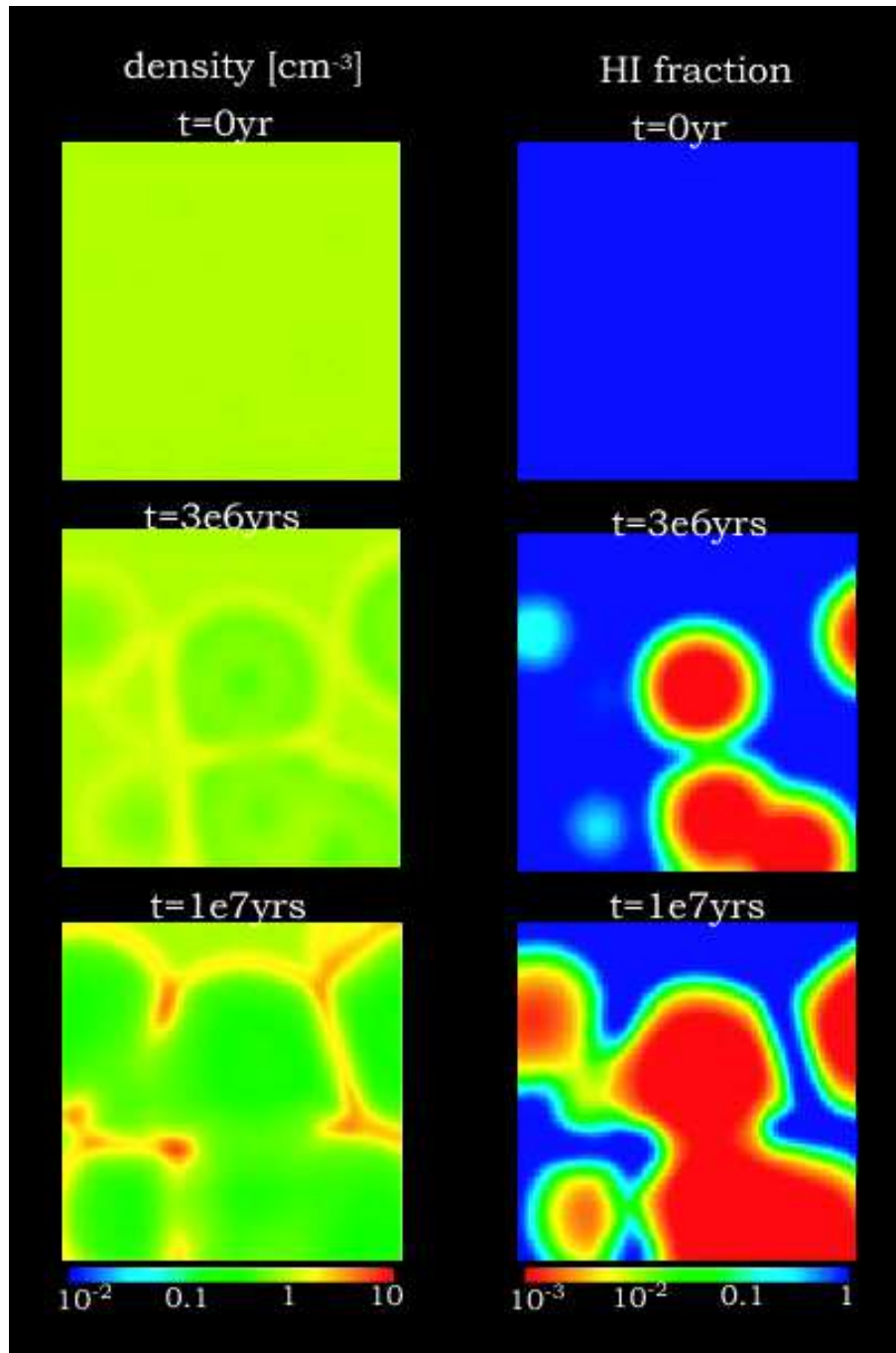


Fig. 9. Spatial slice of the multi-source run in section 3.3 is shown. Left panels show the evolution of density, and the ionization structures are shown in the right panels. The color legends are shown at the bottom.

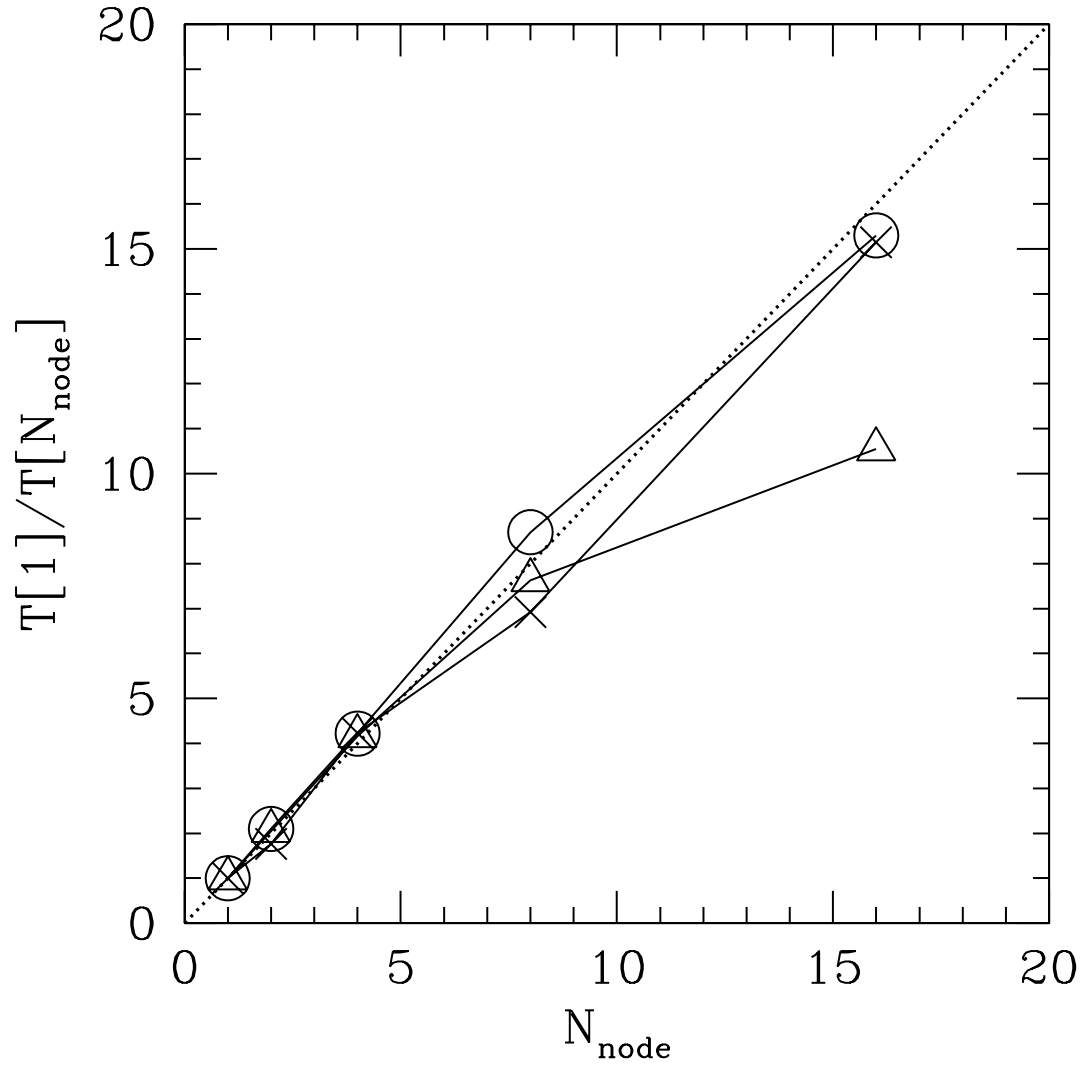


Fig. 10. Speedup of calculations by parallelization is shown. Vertical axis denotes the clock time for one node (two processors) divided by the clock time with N_{node} nodes. Horizontal axis shows the number of nodes. The dotted line represents the case of ideal speedup. Symbols connected by the solid lines are the results with different number of sources (N_{source}): open circles show the results for $N_{\text{source}} = 20$, vertices for $N_{\text{source}} = 10$, and triangles for $N_{\text{source}} = 2$.